34th AIAA Fluid Dynamics Conference and Exhibit, June 28–July 1, 2004/Portland, OR

DNS of Hypersonic Turbulent Boundary Layers

M. Pino Martin*

Department of Mechanical and Aerospace Engineering

Princeton University, Princeton, NJ 08544

We present a direct numerical simulation database of supersonic and hypersonic turbulent boundary layers. The systematic procedure for initializing the turbulent flow fields at controlled Mach number and Reynolds number conditions is described. It is shown that simulation transients are less than 10% of the time required for gathering statistical data of the turbulent flows. The experimental conditions of Debièvе[1,2] and Elena[3,4] are simulated. The magnitude of velocity and temperature fluctuations, as well as the turbulent shear stresses given by the direct numerical simulations are in excellent agreement with the experimental data. Using the direct numerical simulation database we perform parametric studies varying freestream Mach number in the range of 3 to 8 and wall-temperature condition for wall-to-freestream-temperature ratio of 2 to 5.5.

I. Introduction

The study of high-speed boundary layers is important in advancing supersonic and hypersonic flight technology. In a high-speed boundary layer, the kinetic energy is substantial and the dissipation due to the presence of the wall leads to large increases in the temperature. Therefore, a high-speed boundary layer differs from an incompressible one in that the temperature gradients are significant. Since the pressure remains nearly constant across the boundary layer, the density decreases where the temperature increases. Thus, to accommodate for an equivalent mass-flux, a supersonic boundary layer must grow faster than a subsonic one. The extra growth modifies the freestream, and the interaction between the inviscid freestream and the viscous boundary layer affects the wall-pressure distribution, the skin friction and the heat transfer. Furthermore, the high temperature in the boundary layer leads to air reactions. To improve our understanding of the flow physics and to calibrate turbulence models, we need accurate experimental and computational databases of high-speed turbulent boundary layers.

Direct numerical simulations (DNS) provide a vast amount of accurate data that can be used to analyze turbulent boundary layers at high Mach numbers. Based on a better understanding of the real flow physics and using DNS data, accurate turbulence models for high-speed flows can be developed, calibrated, and tested. Recent advances show that building a detailed DNS database of fundamental flows at supersonic and hypersonic conditions is attainable. For example, Guarini et al.[5] perform a DNS of a Mach 2.5 boundary layer at Re_θ=1577; Adams[6] performs a DNS of the turbulent boundary layer over a compression ramp at Mach 3 and Re_θ=1685; Martin[7] performs DNS of turbulent boundary layers at Mach 4 and Re_θ=7225 and 9480 with different wall temperatures; Xu & Martin[8] study the effect of inflow conditions in compressible turbulent boundary layers with Re_θ up to 12,800; and Martin & Candler[9,10] perform DNS of reacting boundary layers at Mach 4. One of the achievements of this DNS work is the ability to accurately simulate

*Assistant Professor, pmartin@princeton.edu

turbulent flows at high Mach numbers while reproducing complex flow physics, shock waves and chemical non-equilibrium effects, permitting the study of turbulence under different flow conditions.

In this paper, we present a DNS database of non-reacting, hypersonic turbulent boundary layers. The governing equations and numerical method are introduced first. We present an initialization procedure to minimize transients while matching the desired skin friction and Reynolds number. We describe the evolution from the initial condition to the realistic turbulent state. We then compare the simulations with available experimental data and assess the accuracy of the DNS database. Finally, we present the results of parametric studies varying the boundary layer edge Mach number and wall-temperature conditions.

II. Governing Equations

The equations describing the unsteady motion of a perfect gas flow are given by the mass, momentum, and total energy conservation equations

$$\frac{\partial \rho}{\partial t} + \frac{\partial}{\partial x_j}(\rho u_j) = 0, \tag{1}$$

$$\frac{\partial \rho u_i}{\partial t} + \frac{\partial}{\partial x_j}(\rho u_i u_j + p\delta_{ij} - \sigma_{ij}) = 0, \tag{2}$$

$$\frac{\partial \rho e}{\partial t} + \frac{\partial}{\partial x_j}\Big(\big(\rho e + p\big)u_j - u_i\sigma_{ij} + q_j\Big) = 0, \tag{3}$$

where ρ is the density; u_j is the velocity in the j direction; p is the pressure; and σ_{ij} is the shear stress tensor given by a linear stress-strain relationship

$$\sigma_{ij} = 2\mu S_{ij} - \frac{2}{3}\mu\delta_{ij}S_{kk}, \tag{4}$$

where $S_{ij} = \frac{1}{2}(\partial u_i/\partial x_j + \partial u_j/\partial x_i)$ is the strain rate tensor, μ is the temperature dependent viscosity and is computed using a power law; and q_j is the heat flux due to temperature gradients

$$q_j = -\kappa\frac{\partial T}{\partial x_j}\ , \tag{5}$$

where κ is the temperature dependent thermal conductivity; and e is the total energy per unit mass given by

$$e = c_v T + \tfrac{1}{2}u_i u_i, \tag{6}$$

where c_v is the assumed constant specific heat at constant volume.

III. Numerical Method

The numerical method combines a weighted essentially non-oscillatory (WENO) scheme for the inviscid fluxes with an implicit time advancement technique. The third-order accurate, high-bandwidth, WENO scheme was designed for low dissipation and high bandwidth[11] and provides shock-capturing, which is necessary at the Mach numbers that we consider. The time advancement technique is based on the Data-Parallel Lower-Upper (DP-LUR) relaxation method[12] that has been extended to second-order accuracy.[13] The derivatives required for the viscous terms are evaluated using 4th-order central differences. We use supersonic boundary conditions in the freestream and periodic boundary conditions in the spanwise direction. As inflow conditions, we use either periodicity in the streamwise direction or prescribed inflow conditions,[8] which results in temporally developing (TDNS) or spatial simulations (SDNS), respectively. The validity of periodic boundary conditions is briefly discussed in this paper. A more detailed discussion can be found in Xu and Martin.[8]

IV. Initialization Procedure

To initialize the turbulent flow, we must prescribe the mean variables and their turbulent fluctuations. The mean flow can be obtained from theory or from a Reynolds-averaged Navier-Stokes (RANS) calculation with different degrees of accuracy depending on the flow conditions. Generally, the prescription of turbulence disturbances is done using random-like perturbations with a flat frequency spectrum or white noise. Then, the initial flow is evolved to a realistic field in time during the DNS, as the shape of the energy spectra and the turbulence structures develop into realistic ones.

The initial flow is considered transitional if we start with a laminar mean flow and small-magnitude perturbations. Then, we can obtain the desired Reynolds number by marching the initial flow field downstream during a DNS. This procedure is costly depending on the desired final turbulent conditions. In contrast, if the initial mean flow is turbulent, we might reach a realistic turbulent flow field with a shorter simulation transient. The caveat here is that non-physically-prescribed-frequency-distributed perturbations might lead to either uncontrolled final realistic conditions (when the flow reaches realistic conditions at a higher-than-desired Reynolds number) or numerical instabilities that prevent the simulation from running. The former constrain increases with freestream Mach number, as the non-linear character of the governing equations is more apparent.

In the present work, we have developed an alternative procedure to initialize the simulations at the desired conditions, matching Mach number, Reynolds number, and boundary conditions. The resulting initial turbulent fields have nearly realistic attributes: mean flow, statistics, energy spectra, and turbulence structure. In turn, the simulation transients are short, numerical instabilities are avoided, and the turbulence conditions at the onset of realistic turbulence can be controlled.

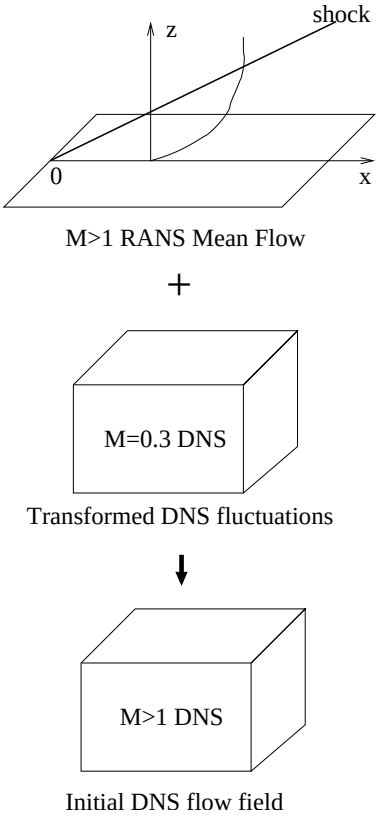

Figure 1. Schematic of the initialization procedure for the direct numerical simulation of turbulent boundary layers.

Figure 1 plots a schematic of the initialization procedure. We first obtain the mean turbulent flow using a Baldwin-Lomax Reynolds-averaged Navier-Stokes simulation.[14] The RANS mean flow carries the Mach, Re_θ, and boundary condition information. We obtain the fluctuating velocity field by transforming the turbulence field of a DNS at $M = 0.3$.[15] Finally, we use the strong Reynolds analogy[16] to calculate the fluctuations in the thermodynamic variables. Details about this procedure are given below.

A. Initial Mean Flow

We perform RANS calculations of freestream flow over a flat plate. Then, we select the mean flow at the desired Re_θ from the corresponding downstream location on the plate. Grid convergence studies are performed and the van-Driest transformed velocity profiles, Reynolds number Re_θ, and the skin friction C_f are compared against the theoretical predictions. Errors in these quantities are washed out during the DNS simulation transient, which is longer with decreasing initial accuracy of the RANS mean flow profiles.

In the present study, we perform two parametric studies with varying freestream Mach number and wall-temperature conditions. For all RANS calculations, the freestream conditions are atmospheric at 20 km altitude. The Reynolds numbers for the mean flow profiles to be selected downstream are based on the maximum values for which we can gather DNS statistics in a reasonable number of days. With this criteria, we compute a typical DNS simulation in roughly three days using 45% of the current computational resources

Case	M_∞	ρ_∞ (kg/m^3)	T_∞ (K)	T_w/T_∞	Re_θ
M2	2.32	0.0970	141.10	1.97	4200
M3	3.00	0.0889	216.65	2.66	2297
M4	4.00	0.0889	216.65	3.88	3767
M5	5.00	0.0889	216.65	5.50	5392
M6	6.00	0.0889	216.65	7.48	7472
M7	7.00	0.0889	216.65	9.82	9932
M8	8.00	0.0889	216.65	12.52	12583
M5T2	5.00	0.0889	216.65	2.0	1691
M5T3	5.00	0.0889	216.65	3.0	2697
M5T4	5.00	0.0889	216.65	4.0	3713
M5T5	5.00	0.0889	216.65	5.5	5392

Table 1. Freestream flow, wall-temperature, and boundary layer profile conditions for the RANS calculations

in the CROCCO Laboratory at Princeton University.[17] As described in the next Section, the number of grid points required for accurate DNS depends on $\delta^+ = \delta/u_\tau$, where δ is the boundary layer thickness and u_τ is the friction velocity. For the current simulations δ^+ is roughly 400, which leads to the selection of the downstream location of the RANS mean flow profile.

Table 1 lists the freestream and wall-temperature conditions for the RANS calculations, as well as Re_θ and δ^+ for the mean profiles that are extracted from each calculation. Case M2 matches existing experimental conditions[1,2,18] and is included for comparison and validation of the numerical data. We use isothermal wall-conditions for all calculations. For the Mach number parametric studies the wall temperature, T_w, is prescribed to be nearly the adiabatic temperature. Figure 2 plots the van-Driest transformed velocity profiles for the RANS calculations. The velocity profiles are more accurate for the nearly adiabatic conditions. The error in C_f relative to the van Driest II[19] predictions is less that 8% for the calculations. As we show in the next Section, this degree of innacuracy leads to simulation transients that are less than 10% of the DNS time that is required to gather statistics.

B. Initial Turbulence Fluctuations

To initialize the velocity fluctuations, we use the turbulent flow field of an incompressible DNS.[15] We assume that (1) the velocity fluctuations are scaled under Morkovin transformation, and (2) the near-wall turbulence structure is similar when visualized in wall units. These assumptions need not be true, they are simply used to obtained an estimate for the initial turbulent fluctuations. Then, the fluctuating velocity field is obtained by normalizing the velocity fluctuations from the incompressible DNS using Morkovin's scaling. Namely,

$$\left(\sqrt{\frac{\overline{\rho}}{\overline{\rho}_w}}\frac{u_i'}{u_\tau}\right)_{M>1} = \left(\sqrt{\frac{\overline{\rho}}{\overline{\rho}_w}}\frac{u_i'}{u_\tau}\right)_{M=0.3}, \tag{7}$$

where $\overline{\rho}_w$ is the mean density at the wall and all variables are evaluated at the corresponding normalized wall-normal location, z^+. An alternative initialization using different normalization factors that include

inner and outer scalings is possible but made no difference in the DNS transient length and resulting data. The initial fluctuations in the thermodynamic variables are estimated using the strong Reynolds analogy[16] and assuming that pressure fluctuations are negligible in a turbulent boundary layer. Thus,

$$T' = -b(\gamma-1)M^2\frac{u'}{\overline{u}}\overline{T}\,, \tag{8}$$

$$\frac{\rho'}{\overline{\rho}} = -\frac{T'}{\overline{T}}\,, \tag{9}$$

where $b = \min(0.8, b_{T>0})$ is a constant conditional proportionality factor that ensures the positiveness of T everywhere in the flow field. In the wall-normal direction, the fluctuations are filtered using a hyperbolic-tangent function

$$f(z^+) = \frac{1}{2}\left\{1+\tanh\left[\frac{3}{2}\left(\frac{z^+ - z^+_{\rm mid}}{z^+_{\rm wake}-z^+_{\rm log}}\right)\right]\right\} \tag{10}$$

where $z^+_{\rm log} = 0.2\delta$, $z^+_{\rm wake} = 0.5\delta$, and $z^+_{\rm mid} = 0.5(z^+_{\rm log}+z^+_{\rm wake})$, so that there are no initial fluctuations outside of the boundary layer.

Figure 3a plots the Morkovin-scaled velocity fluctuations for the Mach 0.3 DNS and an initial flow field at Mach 5. The magnitude of the turbulent velocity fluctuations for the Mach 5 case is modified from that of the Mach 0.3 flow by the filter function, Eq. (10). With this initial condition, we do not expect that the magnitude of the velocity fluctuations is realistic all throughout the boundary layer. However, we have a a good guess of the near wall turbulence magnitude, and no fluctuations outside of the boundary layer. As it will be shown, the magnitude of the fluctuations adjusts during the DNS transient without altering the flow conditions significantly. Figure 3b plots the magnitude of temperature fluctuations for the same cases. Temperature fluctuations are negligible for the Mach 0.3 case and non-zero for the Mach5 case.

C. Initial Turbulent Flow

Combining the RANS mean profile with the transformed fluctuating field as described above leads to turbulent structures and energy spectra that resemble those of a realistic turbulent boundary layer. Figure 4 plots contours of velocity for the Mach 0.3 DNS data and an initial turbulent field at Mach 5 at $z^+ = 8$. The streaky structure of the near-wall boundary layer is apparent. Figure 5 plots the energy spectra for the Mach 5 initial condition at $z^+ = 8$, and $z/\delta = 0.1$, 0.5, and 1.0. The energy is distributed in a cascade-fashion from large to small structures, resembling that of a realistic turbulent flow. The magnitude of fluctuations is nearly zero for $z/\delta > 0.5$, which is due to the filter function, Eq. (10), that is used to damp the fluctuations near the boundary layer edge.

V. DNS Resolution Requirements and Flow Conditions

The computational domain size and structured grid resolution required for the simulations is determined based on the characteristic large length scale, δ, and the characteristic small, near-wall length scale, z_τ. The computational domain must be large enough to contain a good sample of the large scales. On the other hand, the grid resolution must be fine enough to resolve the near wall structures. The first requirement gives the size of the computational domain, whereas the later one gives an estimate on the grid resolution in wall units. Thus, increasing the ratio of the large to small scale $\delta^+ = \delta/z_\tau$ increases the required number of grid points. Ultimately, grid convergence studies or comparisons with experimental or semi-empirical data will determine the final resolution.

After initializing the turbulent flow fields following the procedure from Section IV, we interpolate and/or apply periodicity when necessary to achieve the desired resolution and domain size. To study the effect of Mach number, the wall temperature T_w was fixed to the nearly adiabatic temperature and the freestream Mach number was varied from 3 to 8. To study the wall-temperature effects, we selected the Mach 5

Case	M_δ	ρ_δ (kg/m^3)	T_δ (K)	T_w/T_δ	Re_θ	θ (mm)	H	δ (mm)
M2	2.32	0.0962	145.02	1.91	4452	0.851	3.7	9.90
M3	2.98	0.0907	219.55	2.58	2390	0.430	5.4	6.04
M4	3.98	0.0923	219.69	3.83	3944	0.523	8.5	9.77
M5	4.97	0.0937	220.97	5.40	6225	0.657	12.2	14.82
M6	5.95	0.0952	221.49	7.32	8433	0.733	16.5	21.00
M7	6.95	0.0963	221.61	9.60	10160	0.778	22.3	28.60
M8	7.95	0.0973	221.46	12.25	13060	0.832	28.2	36.92
M5T2	4.97	0.0890	228.12	1.90	1792	0.190	7.4	3.20
M5T3	4.97	0.0908	224.12	2.89	2785	0.294	8.9	5.93
M5T4	4.97	0.0889	231.73	3.74	4185	0.443	10.1	8.92
M5T5	4.97	0.0937	220.97	5.40	6225	0.657	12.2	14.82

Table 2. Dimensional boundary layer edge and wall parameters for the DNS database.

freestream conditions and varied the ratio of wall to edge temperature T_w/T_δ from 1.0 to 5.5. The turbulent boundary layer conditions for the resulting DNS database are given in Tables 2 and 3. Case M2 corresponds to the experimental conditions of Debièvе[2,1,18] and Elena.[3,4]

VI. Assessment of the DNS Data

A. Initialization transient and Two-Point Autocorrelations

We find that monitoring the temporal evolution of the friction velocity is a good indicator of the onset of equilibrium turbulence for the DNS of turbulent boundary layers. Figure 6a plots the normalized friction velocity versus time for DNS. We observe that there is no appreciable variation in u_τ after roughly 0.12 τ_t, where τ_t is a non-dimensional time given by δ/u_τ at t=0. For the simulations varying wall temperature, Fig. 6b, we observe that the initial transient is longer, roughly 0.25 τ_t. Figure 7 plots the temporal evolution of the energy spectra for the Mach 5 DNS. We observe that the energy distribution has reached equilibrium in the near wall region. However, for $z > 0.5\delta$ the energy spectra still changes. Figure 8 plots the streamwise and spanwise two-point autocorrelations for Case M5. Whereas the computational domain is large enough in the streamwise direction, we observe that there is non-zero spanwise correlation for $z = 0.8\delta$. The results from Figures 7 and 8 are representative of what is found for all cases, and indicate that the DNS statistics might not be accurate near the boundary layer edge. This issue is further discussed below.

At the time at which the friction velocity reaches an statistically stationary value, we start gathering statistics. We gather statistics for one non-dimensional time unit, which corresponds to 75 to 30 δ^*/U_δ units for Cases M2 through M8, and from 60 to 40 δ^*/U_δ units for Cases M5T2 through M5T5. Where δ^* is the displacement thickness and U_δ is the mean velocity at the boundary layer edge. Figure 9 plots the van-Driest transformed velocity profiles for the DNS database. We observe good agreement between the theory and the

Case	δ^+	L_x/δ	L_y/δ	L_z/δ	Δx^+	Δy^+	N_x	N_y	N_z
M2	745	7.1	2.1	16.6	16.0	6.0	328	256	120
M3	325	9.1	2.3	13.8	8.0	3.0	384	256	106
M4	368	7.9	2.0	15.4	7.6	2.8	384	256	110
M5	382	7.4	1.8	14.0	7.4	2.8	384	256	110
M6	396	7.0	1.7	15.3	7.2	2.7	384	256	112
M7	414	6.4	1.6	14.8	7.0	2.6	384	256	112
M8	430	6.0	1.5	15.6	6.8	2.5	384	256	113
M5T2	378	7.9	2.0	15.8	7.8	3.0	384	256	110
M5T3	386	7.5	1.9	16.7	7.7	2.9	384	256	110
M5T4	368	7.8	1.9	16.4	7.5	2.8	384	256	110
M5T5	382	7.4	1.8	14.0	7.4	2.8	384	256	110

Table 3. Grid resolution and domain size for the direct numerical simulations.

data for which the intercept of the logarithmic layer is $C = 5.2$.

B. TDNS versus SDNS

The amount of energy that is present in a supersonic boundary layer and the small streamwise computational lengths that are used in the present simulations, make it possible to use periodic boundary conditions in the streamwise direction. A time developing boundary layer simulation is valid provided that (i) the flow can be considered quasi-steady, i.e. the flow adjusts to its local (in time) conditions much faster than the boundary layer thickness changes, and (ii) for the purposes of gathering statistics, the time sampling is shorter than the time scale for boundary layer growth. A flow that satisfies these conditions evolves slowly and can be viewed as a good approximation of a static station of a boundary layer.[8]

The growth time, adjusting time, and sampling time can be estimated as

$$t_{\text{growth}} = \left(\frac{1}{\overline{\delta}} \frac{d\overline{\delta}}{dt} \right)^{-1} , \quad t_\Lambda = \frac{\overline{\delta}}{U_\delta} , \quad t_{\text{sample}} = \frac{\overline{\delta}}{\overline{u}_\tau} ,$$

respectively. Where $\overline{\delta}$ and $\overline{u}_\tau$ are the averaged boundary layer thickness and wall friction velocity. For the simulations, t_Λ is at least two orders of magnitude smaller than t_{growth}, and t_{sample} is less than t_{growth}. Thus, the temporal development of the boundary layer is negligible during an appropriate data collection time. These premises are further corroborated below.

Figure 10a plots the temporal evolution of the friction velocity for Case M5 using TDNS and SDNS. There is nearly no difference between the two simulations. Figure 10b plots the temporal evolution of Re_θ. As expected, the Reynolds number is maintained during the spatial calculation. In contrast, Re_θ increases by roughly 25% during the temporal simulation. Figure 10c plots the van-Driest transformed

velocity profiles for the same simulations. There is virtually no difference in the two datasets. Figure 10d plots the fluctuating Mach number. The second peak in the profile appears slightly farther from the wall for the TDNS simulations, which is a result of the increase in the Reynolds number during the simulation. For the conditions that we consider, the Reynolds number variation is not significant. Nevertheless, caution should be exercise when applying TDNS in higher Reynolds number flows as well as making conclusions about the statistics near the boundary layer edge. All cases listed in Table 2 are computed with TDNS, as currently our TDNS code is more optimized than that for SDNS.

C. Comparison with Experimental Data

We considered the experimental data compilation in AGARDograph No. 315[18] and concluded that the experimental conditions of Debiève[2,1,18] are the only conditions that we can compute based on our turn-around, run-time criteria. The experiment includes the interaction of a $M = 2.32$, $Re_\theta = 4000$ turbulent boundary layer with a shockwave along a compression corner. For the purpose of validation, we use the experimental data for the boundary layer at $x = 20$ mm upstream of the interaction region. In the experiments, the magnitude of the velocity and temperature fluctuations are measured using constant-current, hot-wire anemometry (CCA). Eléna *et al.*[3] and Eléna & Lacharme[4] perform experiments at nearly the same conditions with $M = 2.32$ and $Re_\theta = 4700$ and obtain measurements using laser Doppler velocimetry (LDV) and CCA. They compare the data with the supersonic constant-temperature, hot-wire anemometer (CTA) measurements of Johnson & Rose,[20] the supersonic experiments of Robinson *et al.*,[21] as well as the subsonic turbulent boundary layer study of Klebanoff.[22]

Figure11 plots the mean flow for the DNS and experimental data. There is good agreement among the data, with a small difference in the near-wall total temperature and in the pressure, which is constant across the boundary layer for the DNS data. Figures 12a and 12b plot the normalized magnitude of velocity and temperature fluctuations, respectively. The agreement is very good for the data in $z/\delta < 0.5$ and there is significant disagreement with the experimental data point at $z/\delta = 0.7$. Figures 13a and 13b show the magnitude of the streamwise and wall-normal velocity fluctuations in comparison to the experiments of Elena, where the data are normalized using the edge and friction velocities respectively. The DNS data is in very good agreement with the experimental measurements through-out the boundary layer, specially with the two-component LDV measurements. The agreement is best for the quantities that are normalized using the edge conditions. Figure 13c plots the normalized turbulent shear stress, $\rho u'w'/\rho_w u_\tau^2$. Relative to Elena's experiments, the DNS predict increasingly higher values of the turbulent shear stress with decreasing distance from the wall. The DNS data agrees well with the other supersonic and subsonic experimental data. Figure 13d plots the intermittency, where F_u is the flatness of velocity. The DNS gives higher intermittency levels. Figures 11 through 13 illustrate the overall good agreement among the experimental and DNS data.

VII. Effect of Mach Number

In this section, we study the effect of Mach number using the direct numerical simulation database, Cases M2 through M8. Figure 14a shows that the magnitude of pressure fluctuations increases with freestream Mach number near the wall, although it is consistently less than 6% of the average pressure, and therefore $P'_{\rm RMS}$ is negligible. The same trend is observed for the total temperature fluctuations. Fig. 14b. Figures 14c and 14d plot the fluctuating and turbulent Mach numbers, M' and M_t respectively,

$$M' = \left\langle \frac{u}{a} \right\rangle - \frac{\langle u \rangle}{\langle a \rangle}, \tag{11}$$

$$M_t = \frac{\sqrt{\langle u_i' u_i' \rangle}}{\langle a \rangle}, \tag{12}$$

where M' takes into account that the local speed of sound also fluctuates. For adiabatic walls, $M' > M_t$. Typically, it is assumed that compressibility effects become important when $M' = 0.3$ and that in adiabatic

boundary layers this value is reached when the freestream Mach number is 4 to 5. From Fig. 14c, we observe higher fluctuating Mach numbers than those previously predicted,[23] where the maximum value of M' is about 0.32 and 0.5 for the freestream Mach 3 and 8 simulations. The turbulent Mach number, Fig. 14d, has a less significant freestream Mach number dependence and the maximum values ranges from about 0.3 to 0.38.

Figure 15 plots temperature contours on streamwise-wall-normal planes. The structures are grainier with increasing freestream Mach number which is due to the Reynolds number difference in the range of conditions chosen. We observe that the flow is less intermittent with increasing M_∞. Figure 16 plots the intermittency factor, $3/F_u$ where F_u is the flatness of the streamwise velocity component. The intermittency is an index of the extent of the entrainment process. Smits & Dussage[23] propose that the onset of intermittency occurs nearer the boundary layer edge as the Mach number increases, and that the intermittent zone becomes thinner as the Mach number increases. From Fig. 16, we observe that the wall-ward extent of the entrainment process decreases with increasing Mach number. We cannot make conclusions on wether the onset of intermittency occurs closer to the boundary layer edge with increasing Mach number.

The near-wall transport mechanisms of turbulence can be observed from the turbulent kinetic energy and vorticity budgets. There are four energy exchange mechanisms that take place in turbulent boundary layers: transport, production, dissipation and diffusion of turbulence. The budget equation for the turbulent kinetic energy is

$$\frac{\partial}{\partial t}(\overline{\rho}\,\widetilde{k}\,) + \widetilde{w}\frac{\partial}{\partial z}(\overline{\rho}\,\widetilde{k}\,) = P + T + \Pi_t + \Pi_d + \phi_{dif} + \phi_{dis} + ST$$

where

$$\begin{aligned}
P &= -\overline{\rho u_i'' w''}\,\frac{\partial \widetilde{u}_i}{\partial z}\,, \\
T &= -\frac{1}{2}\,\frac{\partial}{\partial z}\overline{\rho u_i'' u_i'' w''}\,, \\
\Pi_t &= -\frac{\partial}{\partial z}\overline{w'' p'}\,, \qquad \Pi_d = \overline{p'\frac{\partial u_i''}{\partial x_i}}\,, \\
\phi_{dif} &= \frac{\partial}{\partial z}\overline{u_i'' \sigma_{i2}'}\,, \qquad \phi_{dis} = \overline{\sigma_{ij}'\frac{\partial u_i''}{\partial x_j}}\,, \\
ST &= -\overline{w''}\frac{\partial \overline{p}}{\partial z} + \overline{u_i''}\frac{\partial \overline{\sigma_{ij}}}{\partial x_j} - \overline{\rho}\,\overline{k}\,\frac{\partial \widetilde{w}}{\partial z}\,,
\end{aligned} \tag{13}$$

and P is the production due to the mean gradients, T is the redistribution or transport of turbulent kinetic energy, Π_t is the pressure diffusion, Π_d is the pressure dilatation, ϕ_{dif} is the viscous diffusion, ϕ_{dis} is the viscous dissipation, and the ST represents a group of small terms. The first two appear due to the difference between the Favre and Reynolds averaging, the third one is the dilatation-production term. Figure 17a plots the normalized budget terms for the turbulent kinetic energy. We observe no Mach number dependence, and the dominant region for turbulence production is the buffer region.

Let us now consider the vorticity in the flow field. The total change of vorticity can be written as

$$\frac{D\vec{\omega}}{Dt} = (\vec{\omega}\cdot\nabla)\,\vec{u} - \vec{\omega}\,(\nabla\cdot\vec{u}) + \nabla T \times \nabla S\,,$$

where $\vec{\omega}$ and $\vec{u}$ are the vorticity and velocity vectors respectively, T is the temperature and S is the entropy. The first term on the right hand side is the production of vorticity due to vortex stretching and tilting mechanisms, the second term is due to the compressibility of the flow, and the third term is due to the change in the thermodynamic variables and includes the baroclinic torques.

The budget of spanwise vorticity, Figure 17b, shows increasing stretching and vorticity production near the wall with increasing freestream Mach number. Figure 18 shows contours of spanwise vorticity on streamwise-wall-normal planes. Consistent with Fig. 17b the near wall structures are thinner with increasing

M_∞. Also, the streamwise extent of these structures appears to shorten with increasing M_∞. Figure 19 plots iso-surfaces of the discriminant of the velocity gradient tensor,[24] illustrating the near-wall structures. We observe that indeed the structures are shorter with increasing freestream Mach number. This is further corroborated in Figure 20, which plots the longitudinal and transverse integral scales, Λ_x and Λ_y respectively. These are calculated from the conditional averages for $u'(x)u'(x_i) > 0$ and $v'(y)v'(y_i) > 0$ as

$$\Lambda_x = \left\langle \overline{\int_0^{Lx/2} u'(x)u'(x_i)dx} / \overline{u'^2} \right\rangle \tag{14}$$

$$\Lambda_y = \left\langle \overline{\int_0^{Ly/2} v'(y)v'(y_i)dy} / \overline{v'^2} \right\rangle . \tag{15}$$

The structures are largest in the buffer region and the structure extent is of $\mathcal{O}(\delta)$ in the streamwise direction and are about 90 to 100 wall units apart in the spanwise direction. Both the streamwise and spanwise extent of the structures decrease with increasing M_∞.

Figure 21 plots the correlation coefficient for the fluctuating streamwise velocity and temperature fluctuations showing that the Strong Reynolds Analogy holds for the Mach number range that we consider.

VIII. Effect of Wall Temperature

In this section, we consider the DNS database of turbulent boundary layers with varying wall temperature, Cases M5T2 through M5T5. Figure 22a plots the magnitude of pressure fluctuations, which increases with decreasing T_w. The maximum is about 8% of the average pressure at the wall for Case M5T2. The fluctuations in total temperature are mostly affected near the wall, Fig. 22b. The normalized magnitude of the fluctuation increases with decreasing wall temperature and the maximum is nearly 15% of the total temperature for Case M5T2. Figures 22c and 22d plot M' and M_t, respectively. Both the fluctuating and turbulent Mach numbers increase with decreasing T_w in the near-wall region, with larger values given by M'. Away from the wall, the trend of M' might reverse in that M' appears to decrease with decreasing T_w. This could be a Reynolds number effect as, for the conditions chosen, Re_θ decreases with decreasing wall temperature. Figure Figure 23 plots the intermittency factor for the same simulations. We observe no significant effect of T_w.

Figures 24a through 24e plot the terms in the budget of turbulent kinetic energy for the simulations. We observe that the magnitude of turbulent kinetic energy production, viscous diffusion, turbulent transport, and dissipation decrease with decreasing wall temperature, and the maximum values shift farther away from the wall with decreasing T_w. Figure 24f shows a better collapse of the data when using a coordinate transformation that takes into account the variation in density and temperature across the boundary layer. This transformation is given by

$$\zeta^+ = \int_0^z \frac{\langle\rho\rangle u_\tau}{\langle\mu\rangle}\, dz. \tag{16}$$

The location of the maximum and minimum values of the budget terms is nearly the same for all simulations when plotted versus ζ^+. Similar to incompressible flows, the rest of the terms in the turbulent kinetic energy budget are negligible for all cases, and we find that the dissipation is nearly solenoidal.

Let us consider the mechanisms for the generation of spanwise vorticity. Figures 25a and 25b show the magnitude of the stretching/tilting and compressibility terms plotted versus ζ^+, respectively. The stretching/tilting mechanism is dominant except near $\zeta^+ = 10$. Both production mechanisms decrease with decreasing T_w. For all simulations the baroclinic torque is negligible.

The different wall temperature conditions have different effects on the mean variables, which in turn lead to differences in the turbulent structures. In particular, the wall-cooling is a sink of energy, thus there is more energy dissipated with decreasing wall temperature. In turn, the near-wall region is more quiescent

with decreasing T_w. It is the difference in the mean velocity gradient that affects the location of the buffer-region structure and the turbulence production and dissipation mechanisms. These results are consistent with the flow structure topology shown in Fig. 26, where the structures are visualized using iso-surfaces of the discriminant of the velocity gradient tensor Φ.[24] We observe that the structures are smaller and more chaotic with increasing T_w. This is further corroborated in Fig. 27, which plots the longitudinal and transverse integral scales. The structures are longer and fatter with decreasing wall temperature.

IX. Conclusions

Studying physical phenomena via joint numerical and experimental databases requires controlled inflow conditions. This presents a challenge for numerical simulations, since turbulent flows are highly non-linear and initialization procedures and simulation transients make the final flow conditions difficult to control and costly to obtain if starting from a transitional boundary layer. In this paper, we have presented an initialization procedure that leads to short simulation transients, which is necessary to control the final Re_θ for the simulation. We have applied this procedure to initialize turbulent boundary layers over a wide range of Reynolds number, Mach numbers, and wall-temperature conditions. It has been shown that the procedure leads to controlled flow conditions in less than 10% of the direct numerical simulation time that is required to gather turbulence statistics. Using the new initialization procedure, we have simulated the experimental conditions of Debièvе[1,2] and Elena.[3,4] The magnitude of velocity and temperature fluctuations, as well as the turbulent shear stresses given by the direct numerical simulations are in excellent agreement with the experimental data.

Parametric studies varying the freestream Mach number and the wall temperature are performed. The normalized magnitude of fluctuating pressure and total temperature increase with increasing freestream Mach number. It is found that the pressure fluctuations are negligible, whereas the magnitude of fluctuations in total temperature is found to be as large as 15% of the average for a cold Mach 5 boundary layer. The values of the fluctuating Mach number are larger than those previously proposed.[23] Consistent with previous observations, the extent of the intermittent zone decreases with increasing Mach number, and it is unaffected by the wall temperature. The turbulent kinetic energy mechanisms are nearly unchanged with increasing Mach number and the turbulence production is in the buffer region. In contrast, the magnitude of the turbulent kinetic energy mechanisms decreases with decreasing temperature, and the turbulence production occurs further away from the wall. A better collapse of the data is found when the wall coordinate is modified to take into account the change of the thermodynamic variables. The budget of spanwise vorticity shows increasing stretching and compressibility production with increasing Mach number. The integral length scales show that the extent of the structures is reduced with increasing Mach number. The budgets of spanwise vorticity and the integral scale analysis shows that the near wall is more quiescent with decreasing wall temperature.

X. Acknowledgments

This work was supported by the Air Force Office of Scientific Research under grant AF/F49620-02-1-0361 and the National Science Foundation under grant # CTS-0238390.

References

[1]Debieve, J., Gouin, H., and Gaviglio, J., "Momentum and temperature fluxes in a shock wave-turbulence interaction," *Proceedings ICHMT/IUTAM Symposium on the Structure of Turbulence and Heat and Mass Transfer, Dubrovnik*, 1981.

[2]Debieve, J., *Etude d'une interaction turbulence onde de choc*, Ph.D. thesis, Thèse Université d'Aix Marseille II, Marseille, France, 1983.

[3]Eléna, M., Lacharme, J., and Gaviglio, J., "Comparison of hot-wire and laser doppler anemometry methods in supersonic turbulent boundary layers. In: Dybb, A. & Pfund, P.A. (eds)," *International Symposium on Laser Anemometry. ASME*, 1985.

[4]Eléna, M. and Lacharme, J., "Experimental Study of a supersonic turbulent boundary layer using a laser Doppler anemometer," *Journal Mécanique THéorique et Appliquée*, Vol. 7, 1988, pp. 175–190.

[5]Guarini, S., Moser, R., Shariff, K., and Wray, A., "Direct numerical simulation of supersonic turbulent boundary layer at Mach 2.5," *Journal of Fluid Mechanics*, Vol. 414, 2000, pp. 1–33.

[6]adams, N., "Direct simulation of the turbulent boundary layer along a compression ramp at $M = 3$ and $Re_\theta = 1685$," *Journal of Fluid Mechanics*, Vol. 420, 2000, pp. 47–83.

[7]Martin, M., "Preliminary DNS Database of Hypersonic Turbulent Boundary Layers," *AIAA Paper No. 2003-3726*, 2001.

[8]Xu, S. and Martin, M., "Assessment of Inflow Boundary Conditions for Compressible Turbulent Boundary Layers," *Physics of Fluids. Also AIAA Paper No. 2003-3963*, Vol. 16, No. 7, 2004, pp. 2623–2639.

[9]Martin, M. and Candler, G., "DNS of a Mach 4 boundary layer with chemical reactions," *AIAA Paper No. 2000-0399*, 2000.

[10]Martin, M. and Candler, G., "Temperature fluctuation scaling in reacting boundary layers," *AIAA Paper No. 2001-2717*, 2001.

[11]Weirs, V. and Candler, G., "Optimization of weighted ENO schemes for DNS of compressible turbulence," *AIAA Paper No. 97-1940*, 1997.

[12]Candler, G., Wright, W., and McDonald, J., "Data-Parallel Lower-Upper Relaxation method for reacting flows," *AIAA Journal*, Vol. 32, 1994, pp. 2380–2386.

[13]Olejniczak, D. and Candler, G., "Hybrid finite-difference methods for DNS of compressible turbulent boundary layers," *AIAA Paper No. 96-2086*, 1996.

[14]Wright, M., "DPLR and CFD and Code," *NASA Ames Research Center, Moffett Field, CA*, 2003.

[15]Spalart, P. and Watmuff, J., "Direct Numerical Simulation of a Turbulent Boundary Layer up to $Re_theta = 1410$." *Journal of Fluid Mechanics*, Vol. 187, 1988, pp. 61–98.

[16]Morkovin, M., "Effects of compressibility on turbulent flows," *A.J. (ed) of Mèchanique de la Turbulence, CNRS*, 1962, pp. 367–380.

[17]Laboratory, C., "Cluster for Research on Complex Computations," *croccolab.princeton.edu*, 2002.

[18]Fernholz, H., Finley, P., Dussauge, J., and A.J.Smits, "A survey of measurements and measuring techniques in rapidly distorted compressible turbulent boundary layers," *AGARDograph No. 315*, 1989.

[19]Driest, E. V., "Problem of aerodynamic heating," *Aeronautical Engineering Review*, Vol. 15, 1956, pp. 26–41.

[20]Johnson, D. and Rose, W., "Laser velocimetry and hot-wire anemometer comparison in a supersonic boundary layer," *AIAA Journal*, Vol. 13, 2000, pp. 512–515.

[21]Robinson, S., Seegmiller, M., and Kussoy, M., "Hot-wire and laser Doppler anemometer measurements in a supersonic boundary layer," *AIAA Paper No. 83-1723*, 1983.

[22]Klebanoff, P., "Characteristics of turbulence in a boundary layer with zero pressure gradient," *NASA Report No. 1247*, 1955.

[23]Smits, A. and Dussauge, J., *Boundary Layer Mean-Flow Behavior*, AIP PRESS, 1996, In Turbulent Shear Layers in Supersonic Flows.

[24]Blackburn, H., Mansour, N., and Reynolds, W., "Topology of finite-scale motions in turbulent channel flow," *Journal of Fluid Mechanics*, Vol. 310, 1996, pp. 269–292.

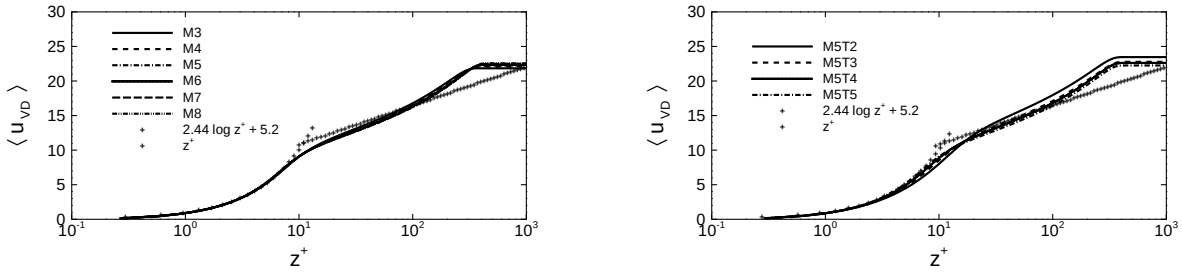

(a) (b)

Figure 2. Initial mean velocity profiles from RANS.

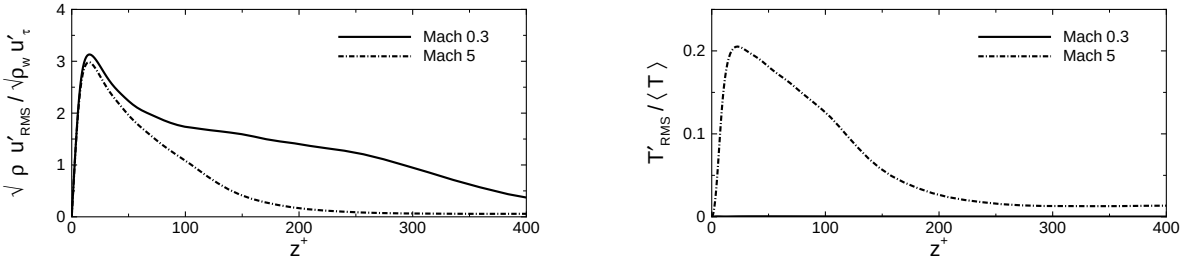

(a) (b)

Figure 3. Initial velocity and temperature fluctuations for a Mach 5 turbulent boundary layer, case M5.

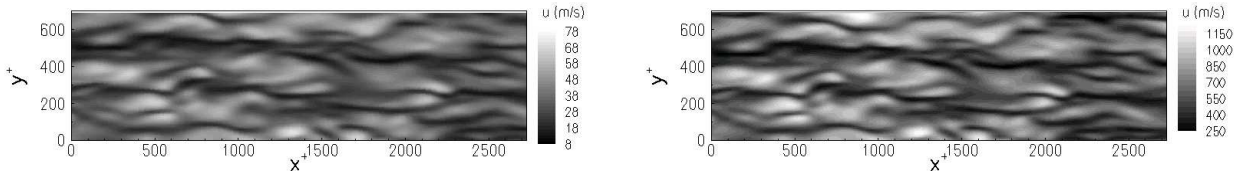

(a) (b)

Figure 4. Velocity contours for the (a) Mach 0.3 and (b) initial Mach 5, Case M5, boundary layer flow field at $z^+ = 8$.

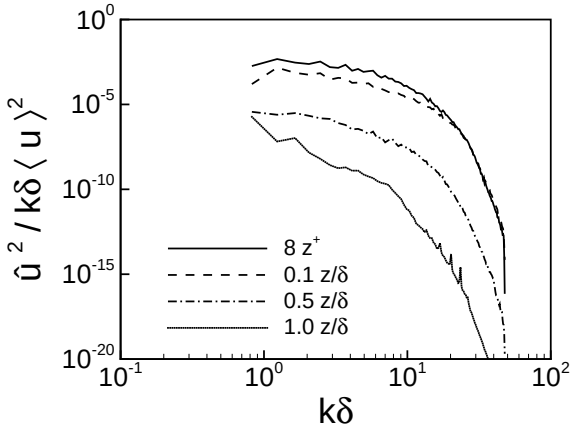

(a)

Figure 5. Initial energy spectra for a Mach 5 turbulent boundary layer, Case M5.

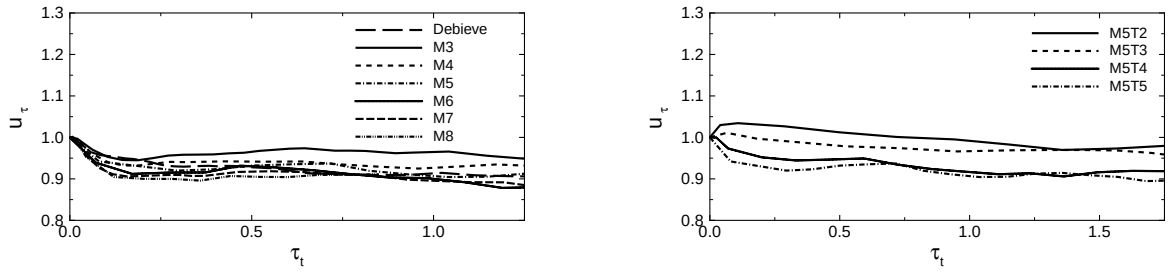

(a) (b)

Figure 6. Temporal evolution of the friction velocity for the DNS of turbulent boundary layers.

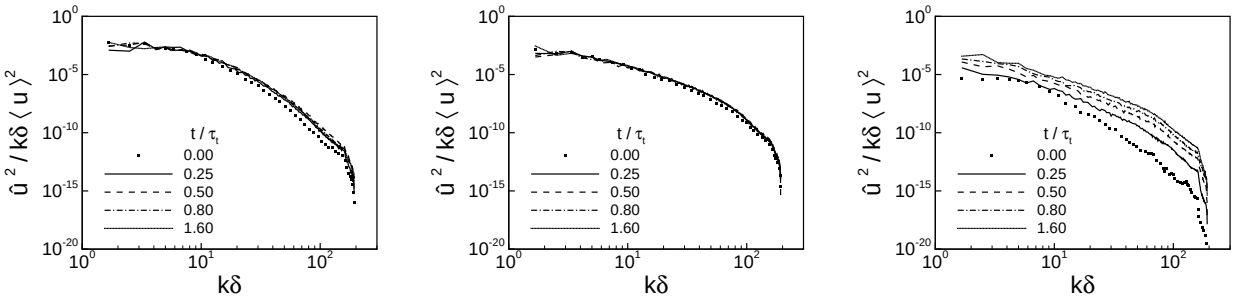

(a) (b) (c)

Figure 7. Non-dimensional energy spectra at (a) $z^+ = 8$, (b) $z/\delta = 0.1$, and (c) $z/\delta = 0.5$ for Case M5.

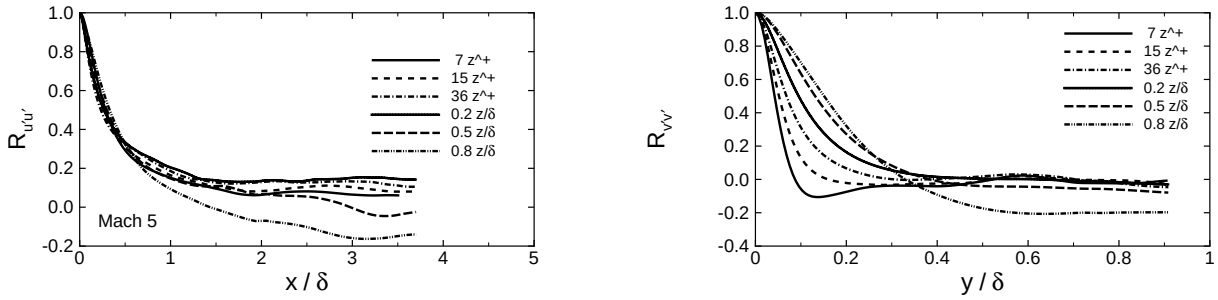

(a) (b)

Figure 8. Streamwise and spanwise two-point correlation for Case M5.

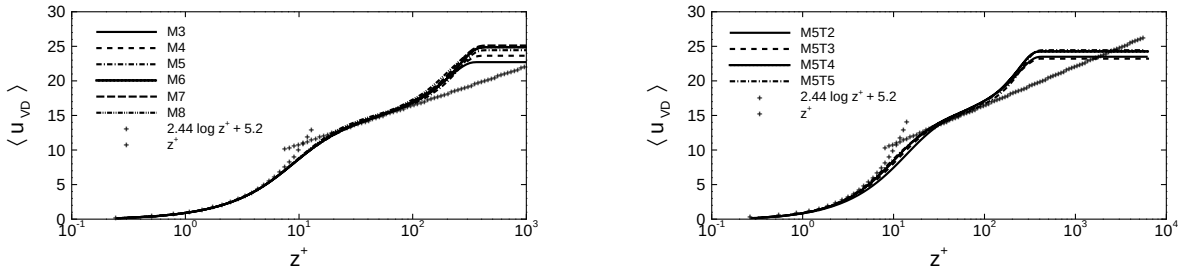

(a) (b)

Figure 9. Mean velocity profiles for the DNS database.

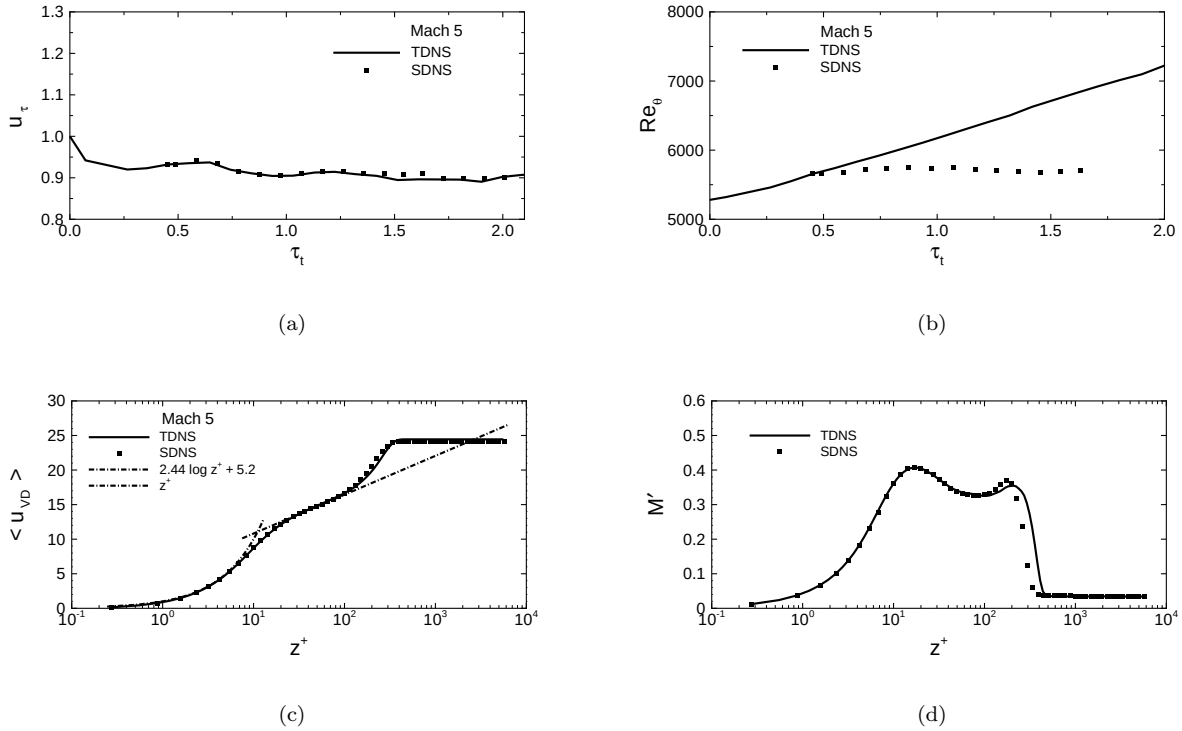

Figure 10. Comparison between TDNS and SDNS for Case M5 (a) temporal evolution of the normalized friction velocity; (b) temporal evolution of Re_θ; (c) van-Driest transformed velocity profile; (d) fluctuating Mach number.

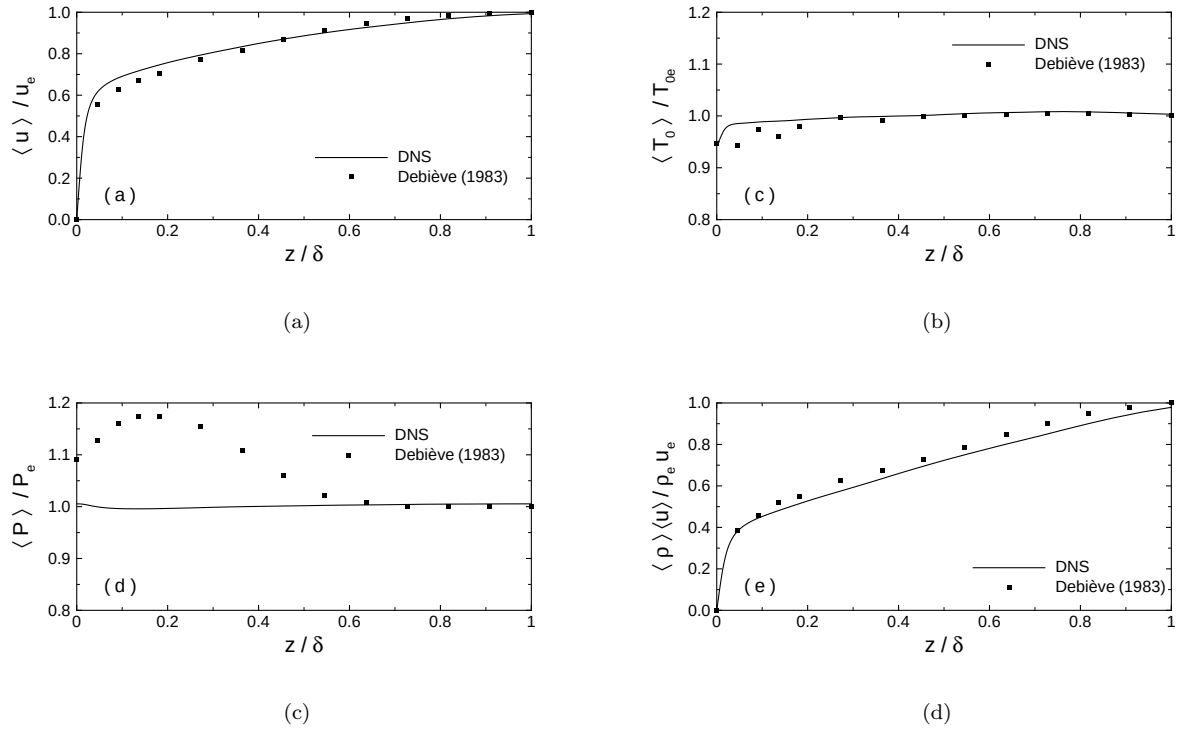

Figure 11. Comparison between DNS Case M2 and experimental data.[2,1,18] Notmalized values of mean (a) velocity; (b) total temperature; (c) pressure; (d) momentum. Quantities are normalized using edge values.

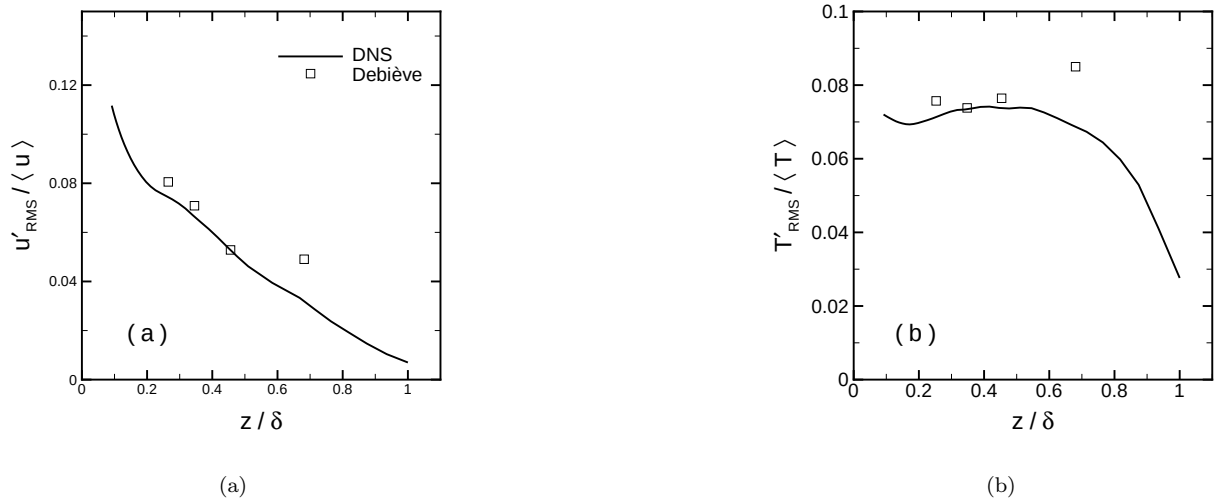

Figure 12. Comparison between DNS Case M2 and experimental data.[2,1,18] (a) Streamwise component of turbulent fluctuations; (b) Turbulent temperature fluctuations. Quantities are normalized using mean flow variables

.

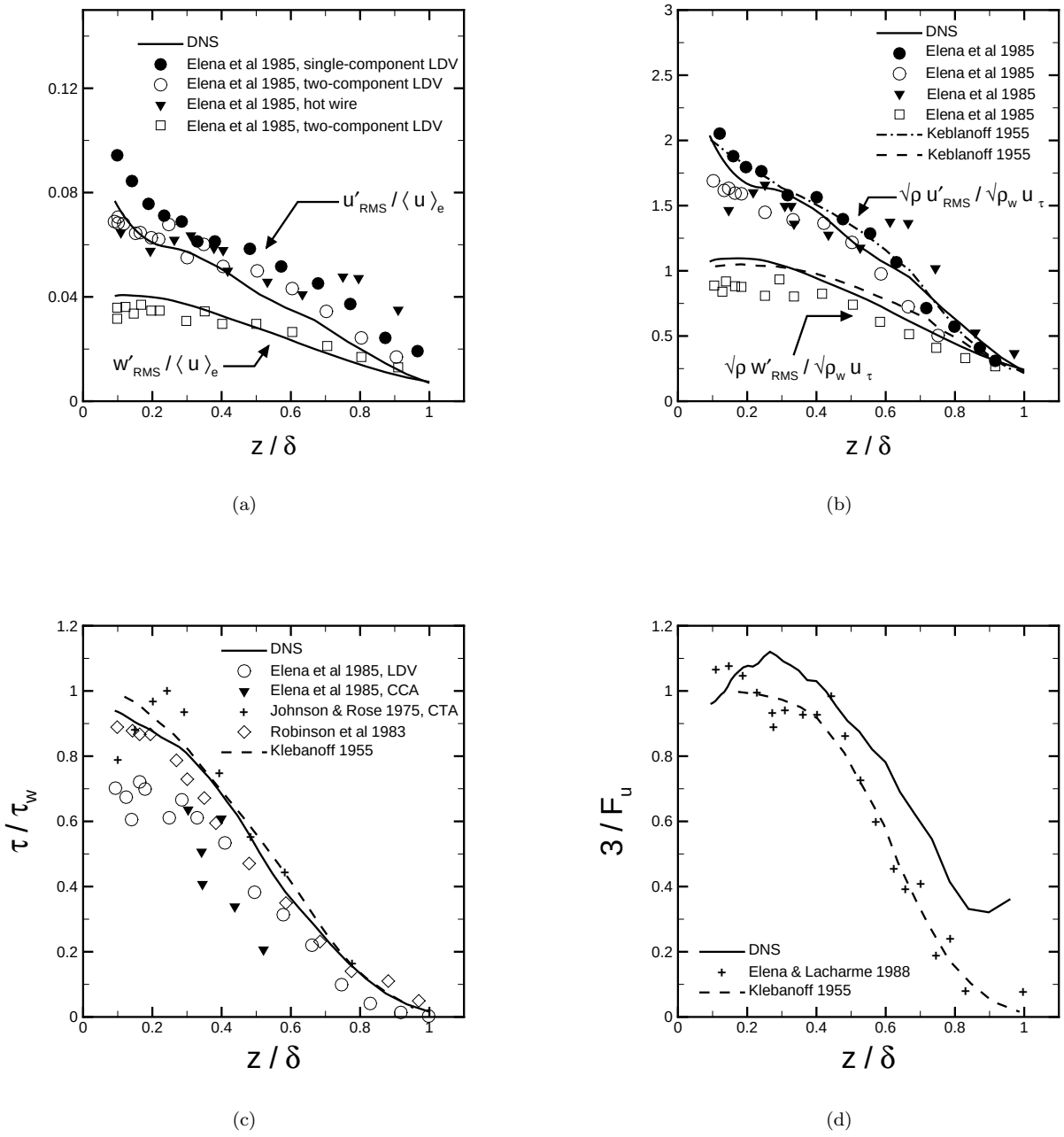

Figure 13. Comparison between DNS Case M2 and experimental data.[3,4,20,21,22] (a) Magnitude of velocity fluctuations normalized with edge velocity; (b) Magnitude of velocity fluctuations normalized with Morkovin's scaling; (c) Normalized turbulent shear stress; (c) Intermittency factor.

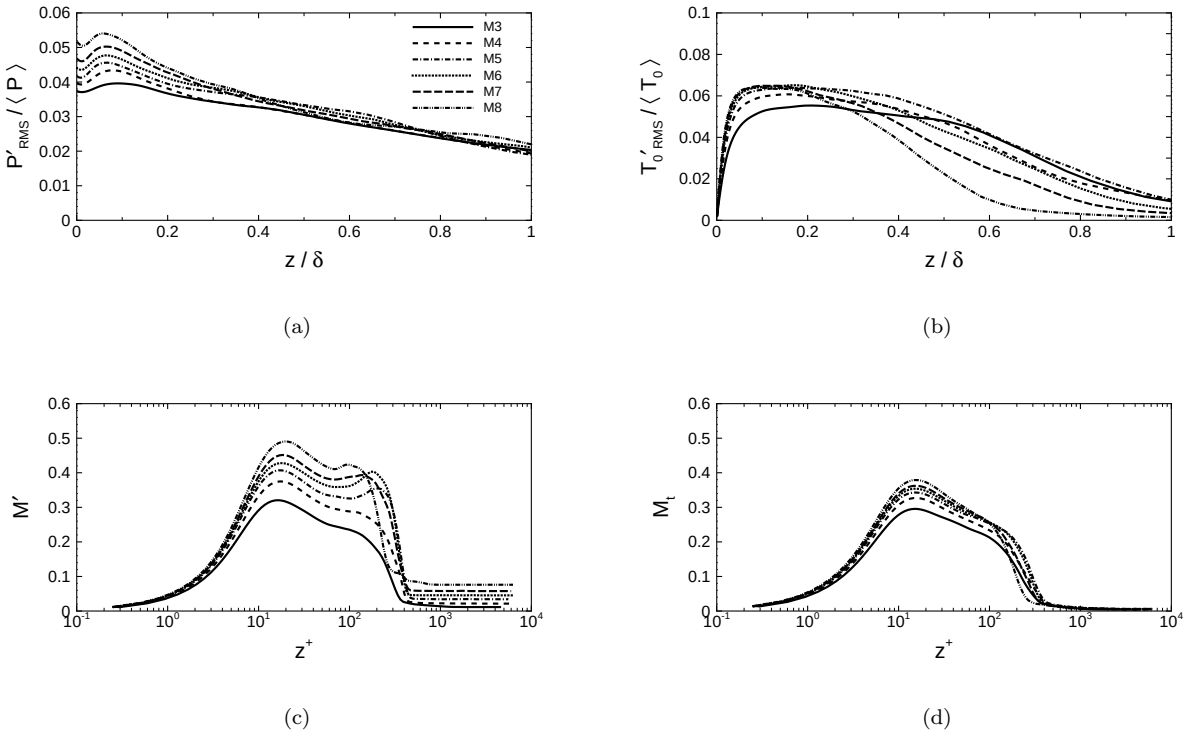

Figure 14. DNS database varying Mach number. (a) Normalized magnitude of pressure fluctuations; (b) Normalized magnitude of total temperature fluctuations; (c) Fluctuating Mach number M'; (d) Turbulent Mach number M_t.

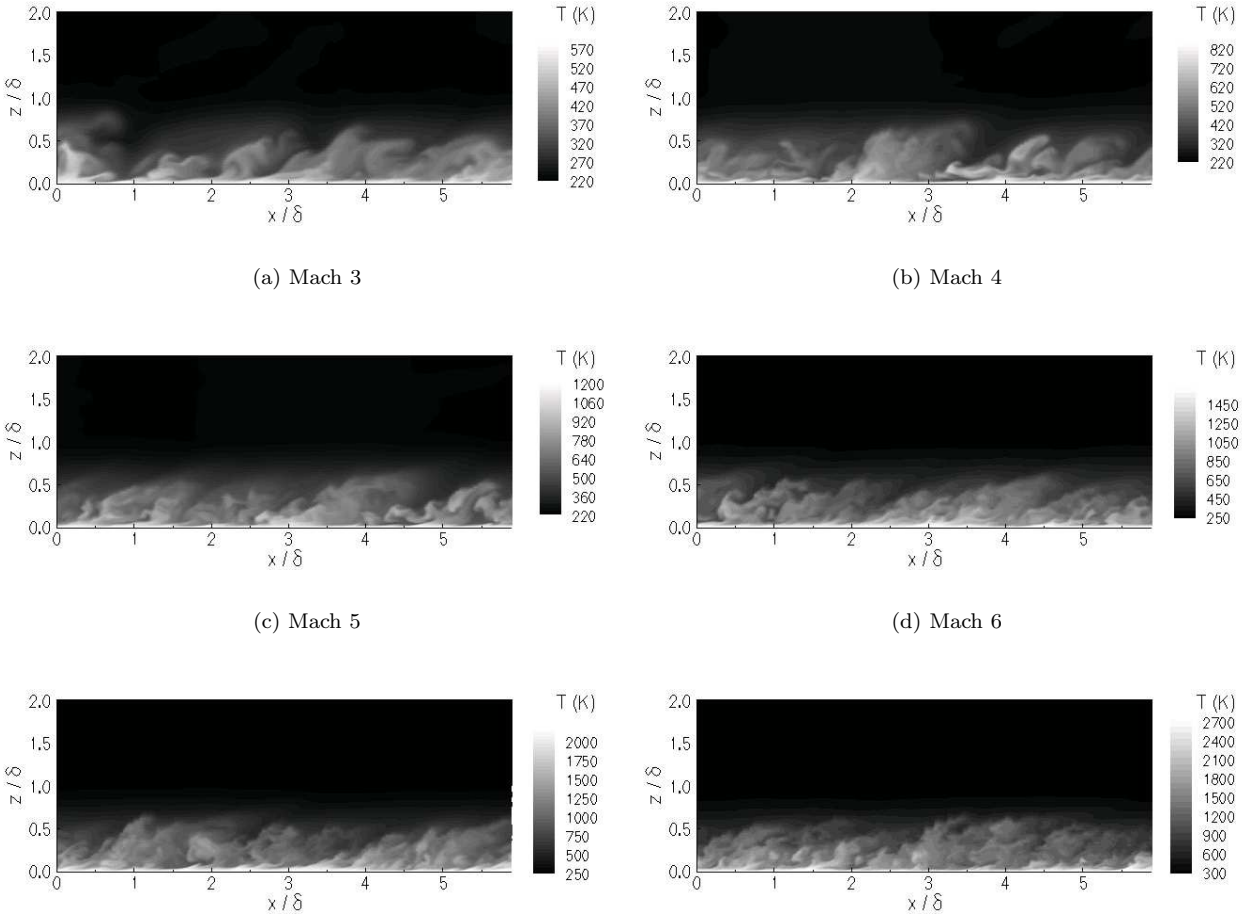

(a) Mach 3

(b) Mach 4

(c) Mach 5

(d) Mach 6

(e) Mach 7

(f) Mach 8

Figure 15. Streamwise-wall-normal temperature contours for the DNS database varying Mach number.

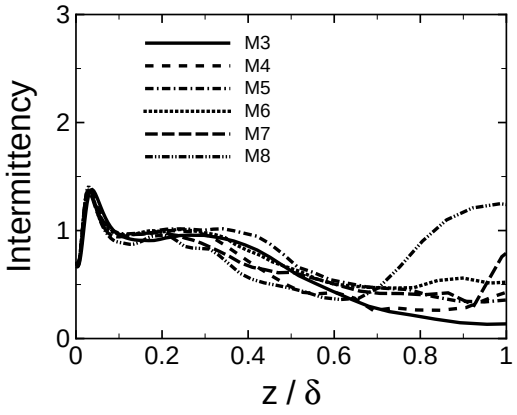

(a)

Figure 16. Intermittency for the DNS database varying Mach number.

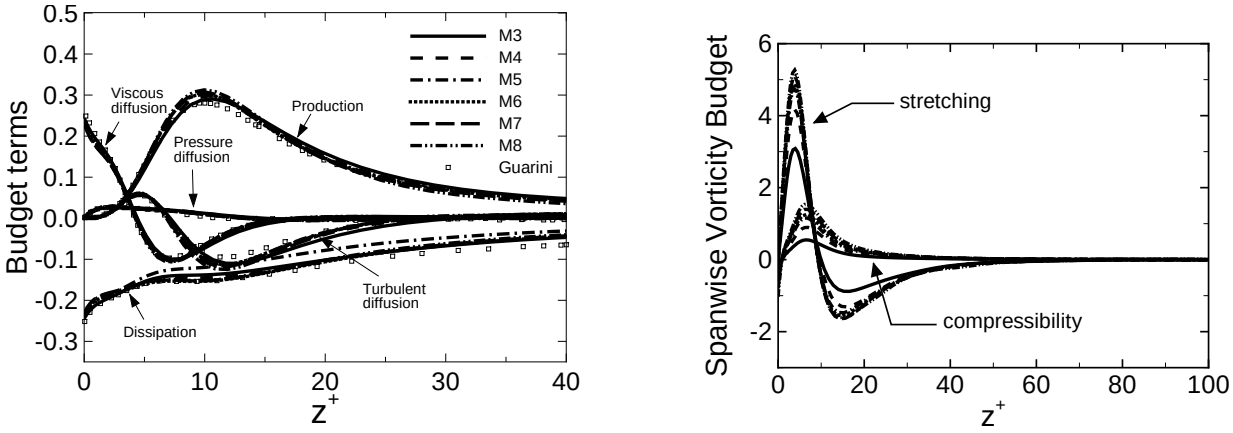

(a) (b)

Figure 17. DNS database varying Mach number. (a) Turbulent kinetic energy budget, where the variables are non-dimensionalized with $u_\tau \tau_w / z_\tau$, $\tau_w = \rho_w u_\tau^2$; (b) Spanwise vorticity budget, where the variables are non-dimensionalized with u_τ and z_τ.

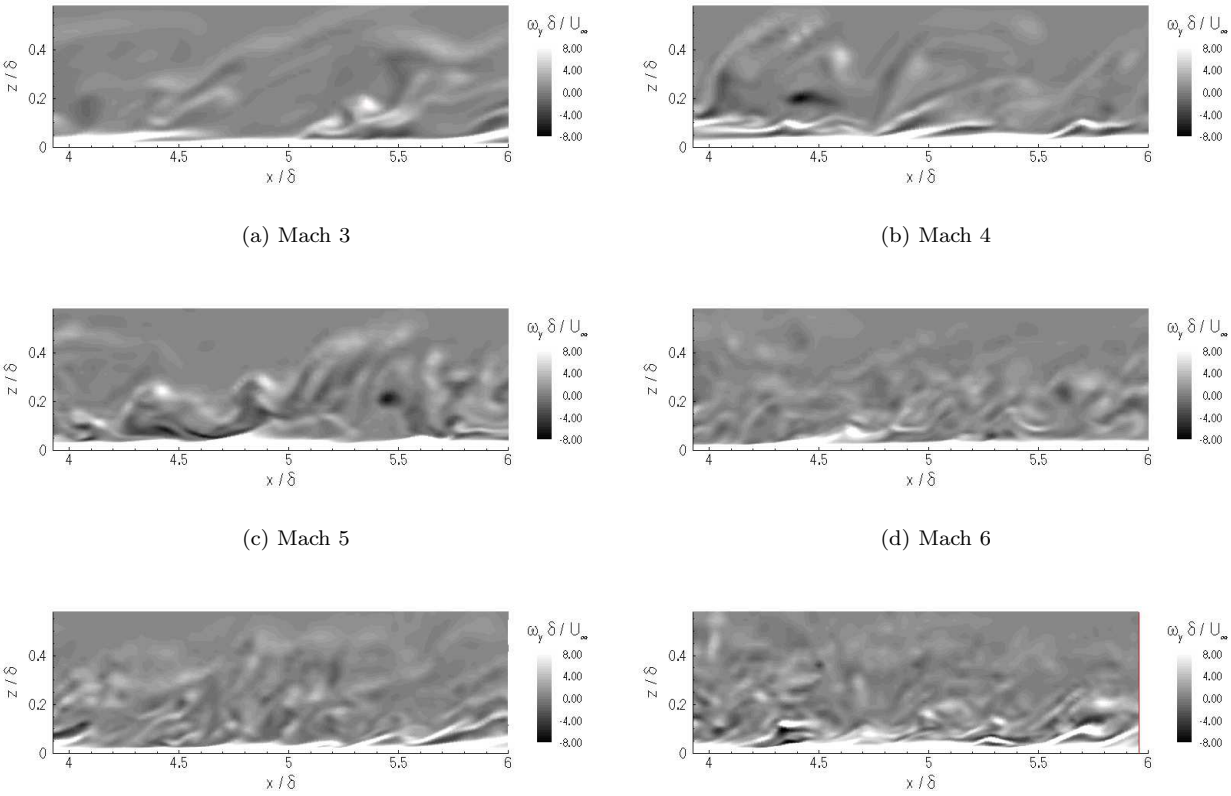

(a) Mach 3

(b) Mach 4

(c) Mach 5

(d) Mach 6

(e) Mach 7

(f) Mach 8

Figure 18. Spanwise-vorticity contours for the DNS database varying Mach number.

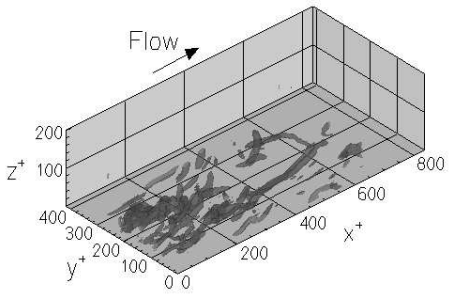

(a) Mach 3

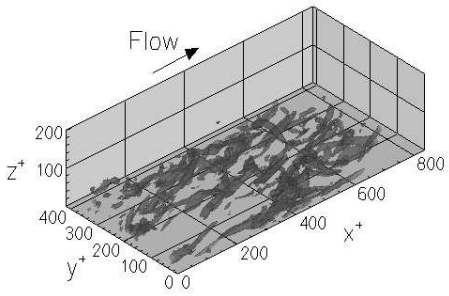

(b) Mach 4

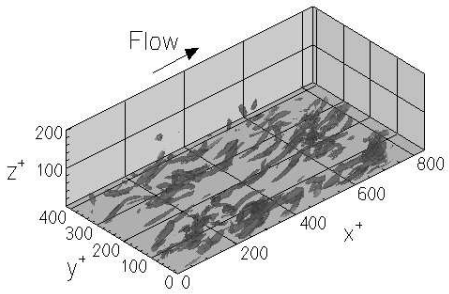

(c) Mach 5

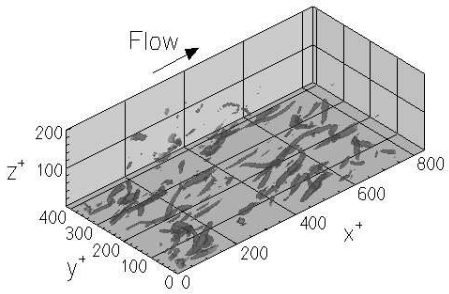

(d) Mach 6

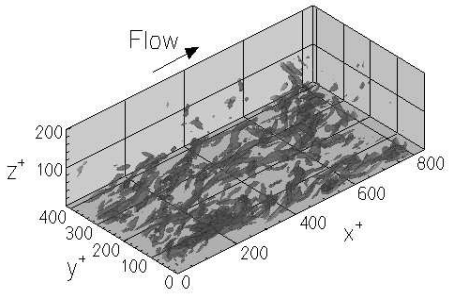

(e) Mach 7

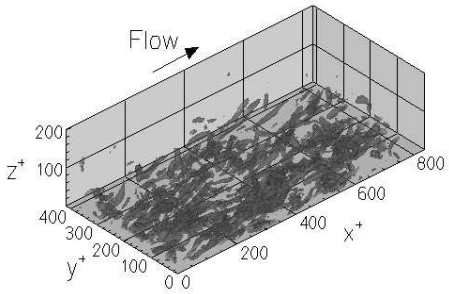

(f) Mach 8

Figure 19. Iso-surface (10^{-4} of maximum value) of the discriminant of the velocity for the DNS database varying Mach number.

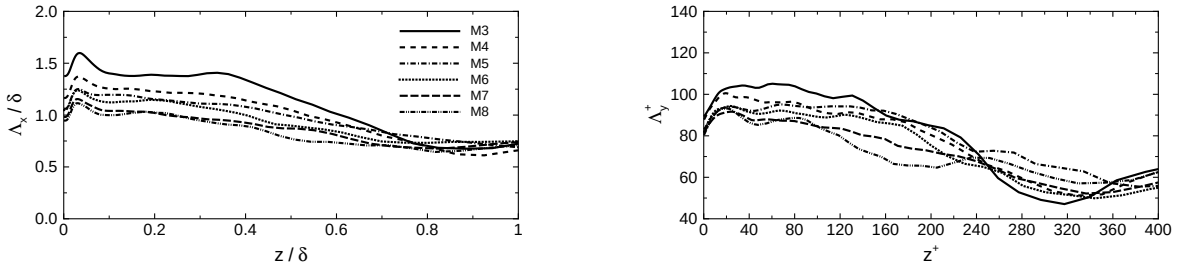

(a) (b)

Figure 20. DNS database varying Mach number. (a) Longitudinal integral length scale Λ_x; (b) Transverse integral length scale Λ_y.

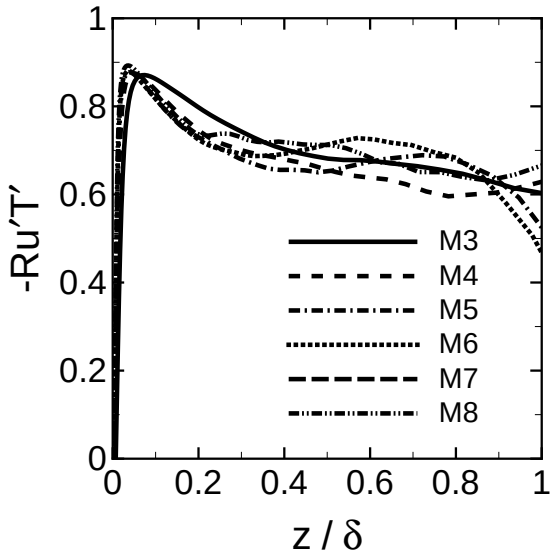

(a)

Figure 21. Fluctuating streamwise velocity and temperature correlation coefficient for the DNS database varying Mach number.

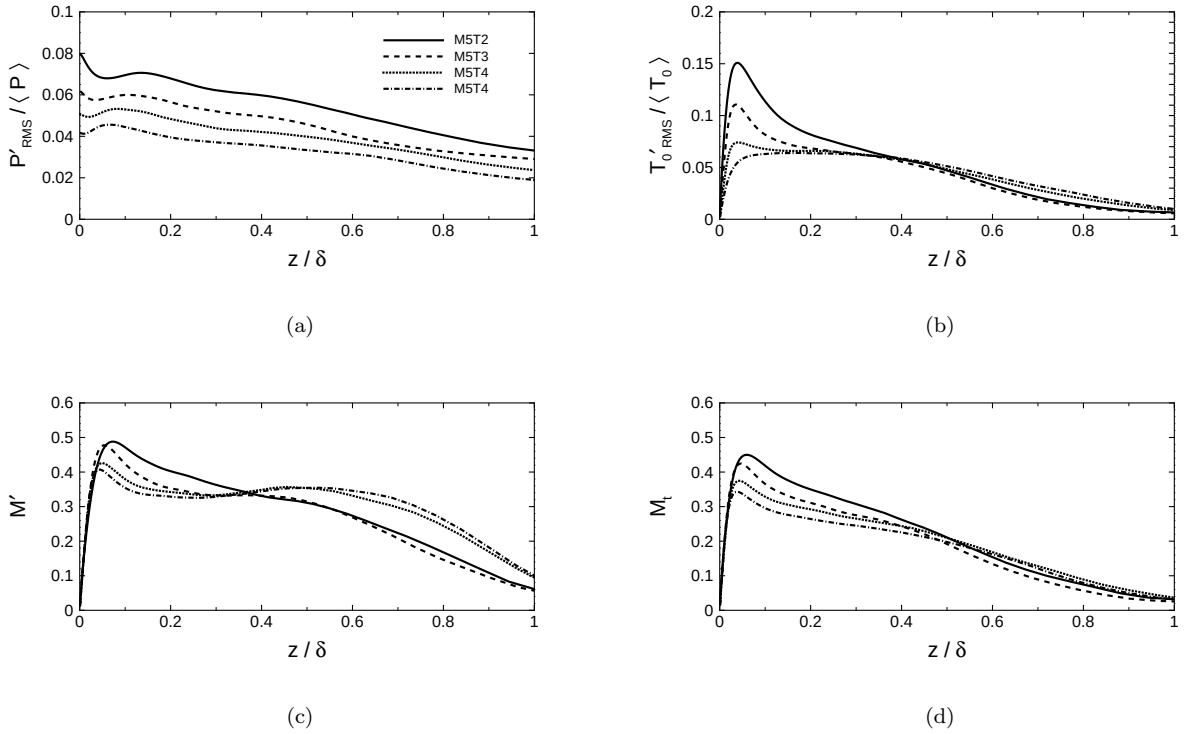

Figure 22. DNS database varying wall temperature. (a) Magnitude of pressure fluctuations; (b) Magnitude of total temperature fluctuations; (c) Fluctuating Mach number M'; (d) Turbulent Mach number M_t.

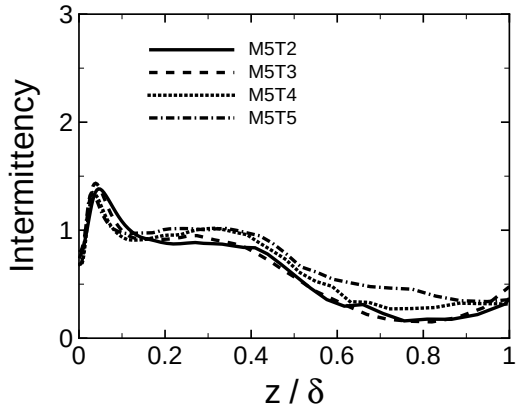

Figure 23. Intermittency for the DNS database varying wall temperature.

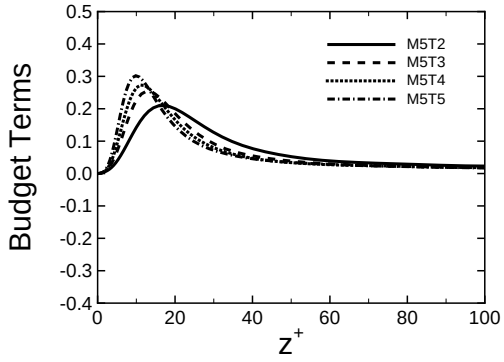

(a) Production

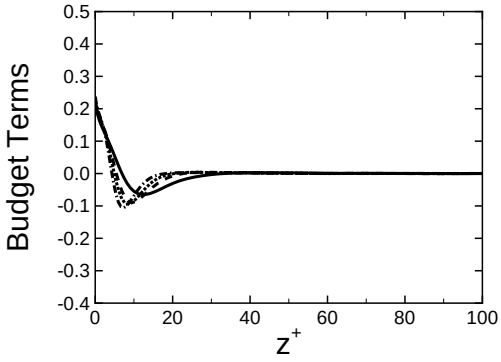

(b) Viscous diffusion

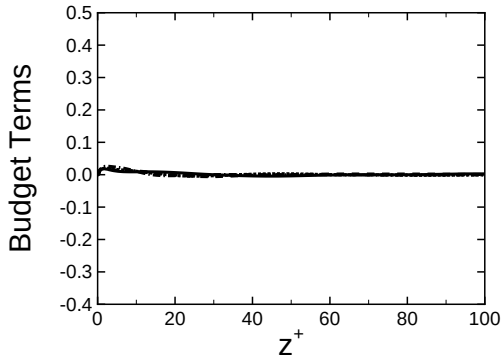

(c) Pressure diffusion

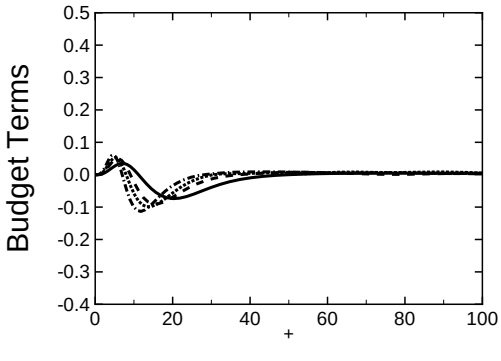

(d) Turbulent transport

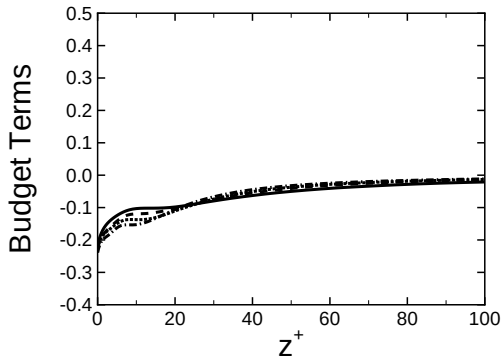

(e) Dissipation

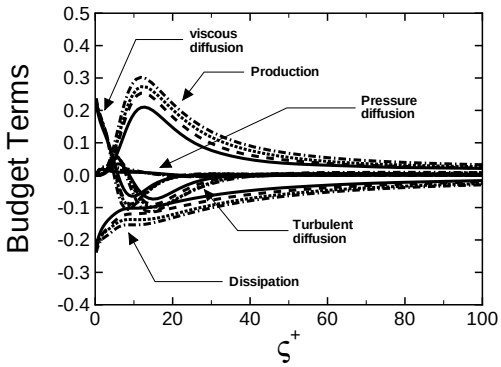

(f) versus ζ^+

Figure 24. Turbulent kinetic energy budget for the DNS database varying wall temperature. The variables are non-dimensionalized with $u_\tau \tau_w / z_\tau$, where $\tau_w = \rho_w u_\tau^2$.

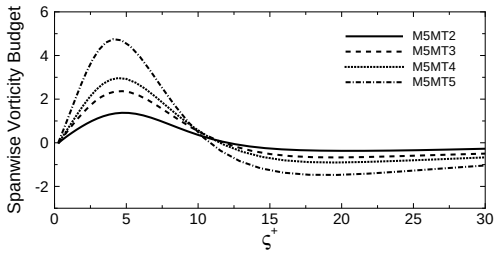

(a) Stretching term

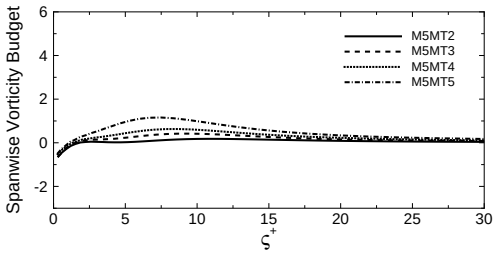

(b) Compressibility term

Figure 25. Spanwise vorticity budget for the DNS database varying wall temperature. Variables are non-dimensionalized with u_τ and z_τ.

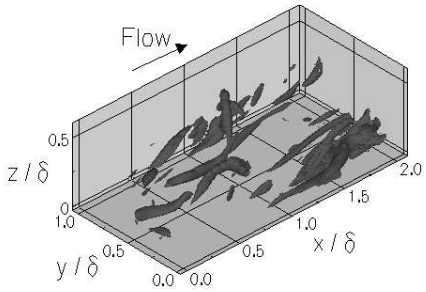

(a) M5T2

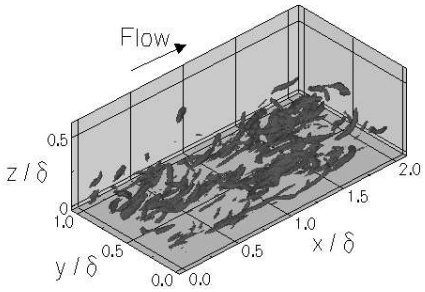

(b) M5T5

Figure 26. Iso-surface, $10^{-4} swirl_{\max}$, of the discriminant of the velocity showing the effect of wall temperature.

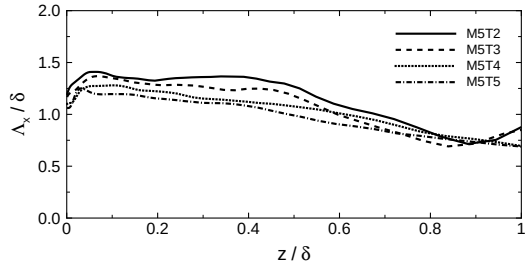

(a)

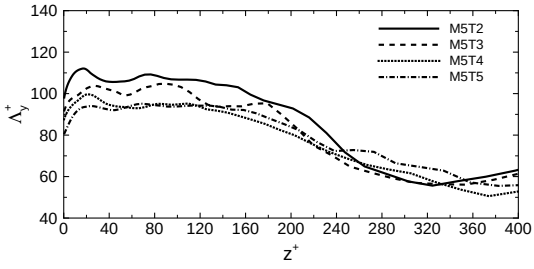

(b)

Figure 27. DNS database varying wall temperature. (a) Longitudinal integral Λ_x; (b) Transverse integral scale Λ_y.